Earth-Science Reviews 281 (2026) 105632

Contents lists available at ScienceDirect

Earth-Science Reviews

journal homepage: www.elsevier.com/locate/earscirev

Review Article

Paleogeographic modulation of Phanerozoic climate by albedo compensation of interhemispheric land imbalances

G. Muttoni [a,*], D.V. Kent [b,c]

[a] Dipartimento di Scienze della Terra "Ardito Desio", Università degli Studi di Milano, via Luigi Mangiagalli 34, I-20133 Milano, Italy
[b] Lamont-Doherty Earth Observatory of Columbia University, Palisades, NY 10964, USA
[c] Department of Earth and Planetary Sciences, Rutgers University, Piscataway, NJ 08854, USA

ARTICLE INFO

Keywords:
Phanerozoic
Paleogeography
Surface reflectivity
Cloud compensation
Absorbed solar flux
Ice ages

ABSTRACT

Earth's climate during the Phanerozoic oscillated between intervals punctuated by a few ice ages (three in the Paleozoic and the current ice age in the Late Cenozoic, corresponding to a cumulative glacial occupancy of ~17% of the eon) to none documented in the intervening ~225-Myr-long interval encompassing the latest Paleozoic, entire Mesozoic, and early Cenozoic, here termed the 'Greater Mesozoic' glacial gap. In this review, we compile and synthesize published paleogeographic reconstructions from 530 Ma to the present to quantify the distribution of land and sea by hemisphere and zonal climate belts and reconstruct surface reflectivity through time. We show that hemispheric asymmetries in land area generated large imbalances in surface albedo that require compensating processes—most plausibly more clouds to increase albedo of the darker, more oceanic hemisphere, as occurs today—to maintain Earth's overall hemispheric radiative symmetry and heat balance. Intervals including glaciations, especially in the Paleozoic but also in the Late Cenozoic, are characterized by high compensated reflectivity and lower absorbed solar flux, calculated from compensated reflectivity and secular solar evolution, while low compensation values and higher absorbed solar flux mark the intervening ~225-Myr-long 'Greater Mesozoic' glacial gap. For example, the contrast between the pre-onset states of the Late Cenozoic and Late Paleozoic ice ages is ~14 W m^{-2}, implying that, even assuming atmospheric damping, the effective climate conditioning remains on the order of CO_2 doubling (or halving) forcings. We therefore propose that glaciations were preferentially triggered under high compensated reflectivity preconditions, corresponding to low absorbed solar flux, which may have reduced the energetic threshold for CO_2-driven ice-sheet initiation, especially when coupled with enhanced CO_2 sink efficiency through continental weathering on equatorial landmasses, including arc–continent collision zones and topographically elevated large continental igneous provinces.

Contents

* Corresponding author.
E-mail address: giovanni.muttoni1@unimi.it (G. Muttoni).

https://doi.org/10.1016/j.earscirev.2026.105632
Received 28 October 2025; Received in revised form 10 July 2026; Accepted 18 July 2026
Available online 20 July 2026
0012-8252/

1. Introduction

Global climate during the Phanerozoic, the past 540 million years (Ma) of Earth history (IUGS, 2024), can be characterized as generally warm, at least free of continental glaciations, interspersed by three or four ice ages representing only about 1/6 of the time (Fig. 1A). The few ice ages are also not uniformly distributed in time. In the Paleozoic Era, the Late Ordovician Hirnantian (H) ice age is the oldest and the shortest (457 to 455 Ma (Bergmann et al., 2025) although perhaps extending into the Silurian to ~440 Ma (Macdonald et al., 2019)); a rather less certain Late Devonian (LD) glaciation (~365–359 Ma, Macdonald et al., 2019); and the longest at ~50-Myr Late Paleozoic ice age (LPIA, 330 to 280 Ma, Montañez, 2022; Montañez and Poulsen, 2013; or up to ~260 Ma; Macdonald et al., 2019) all occurred on continents in high southern hemisphere paleolatitudes. These were followed by a ~225 Myr glaciation-free interval encompassing the latest Paleozoic, the Mesozoic and early Cenozoic, hereafter referred to as the 'Greater Mesozoic' glacial gap, with little to no evidence of ice sheets until the current Late Cenozoic ice age (LCIA) that started at the beginning of the Oligocene (~34 Ma) with Antarctic glaciation at high southern paleolatitudes (DeConto and Pollard, 2003) and eventual evidence of ice in Greenland (Eldrett et al., 2007) leading to bipolar ice sheets by the Quaternary. This is the broad spatiotemporal pattern of climate we seek to explain.

Global climate is driven by solar insolation penetrating the atmosphere as shortwave radiation that is converted to blackbody longwave radiation, which gets absorbed by greenhouse gases with the heat distributed by the coupled ocean-atmosphere system in response to horizontal and vertical gradients created by buoyancy plus Coriolis and tidal forces (Manabe and Broccoli, 2020). The faint young Sun paradigm (Feulner, 2012) points to an increase of about a 1% per ~110 Myr in insolation at the top of the atmosphere during the Phanerozoic (Gough, 1981); there is also the rhythmic spatiotemporal distribution of insolation on annual and orbital (Milankovitch) timescales that can account for climate oscillations over thousands to several millions of years (e.g., Olsen et al., 2019). Planetary albedo, the proportion of insolation reflected back into space, is currently about 0.3 (Stephens et al., 2015); about half is due to cloud cover for which there are no proxies in modern or deep-time climate reconstructions.

Major long-term climate changes tend to be vested in the carbon cycle and resulting variations in atmospheric CO_2 (Berner, 1990; Crowley and Berner, 2001). CO_2 is a greenhouse gas that has constituted several hundred to a few thousand parts per million by volume (ppmv) of the atmosphere as gauged directly by measurements of atmosphere trapped in bubbles in Antarctica ice that now extend back to about 3 Myr (Luthi et al., 2008; Marks-Peterson et al., 2026), of infrequent fluid inclusion results (Lowenstein et al., 2014), and more generally by fossil proxies such as leaf stomata, pedogenic carbonates and boron isotopes (CENCO2PIP_Consortium, 2023; Foster et al., 2017). The available proxy data generally extend back to around 415 Ma with the appearance and spread of land plants in the Siluro–Devonian.

Atmospheric concentrations of CO_2 have also been inferred for the entire Phanerozoic from mass balance carbon-cycle models, notably GEOCARBSULF_volc (Berner, 2006a; Berner, 2006b), COPSE (Lenton et al., 2018), and SCION (Mills et al., 2021) (Fig. 1B). Such carbon-cycle models include both volcanic degassing and CO_2 consumption processes, although long-term atmospheric CO_2 evolution is often considered to be more strongly influenced by variable outgassing inferred from broadly estimated global changes in sea-floor production (Gaffin, 1987; Berner, 1990) and associated subduction through time. However, the best available direct analysis of extant sea floor (Rowley, 2002) indicates no significant long-term trends in the rate of sea-floor production over the past ~180 Myr, although shorter-term fluctuations are evident, and this conclusion extends back to ~240 Ma when deformation along major rifts and collision zones is taken into account (Müller et al., 2019).

If generally valid as null hypothesis, this observation would argue that the average CO_2 input to the ocean–atmosphere system from plate-tectonic sources has remained steady over much longer stretches of geologic time. Long-term changes in atmospheric CO_2 would then be more plausibly linked to variations in CO_2 consumption processes—principally silicate weathering (Walker et al., 1981) and organic carbon burial (Berner, 2003)—rather than to fluctuations in outgassing rates. The silicate weathering feedback acts as the dominant, rapid sink regulating atmospheric CO_2 on multimillion-year timescales. Its efficiency is maximized within the equatorial belt (10° S–10° N), where warm temperatures and intense runoff, especially with topographic relief (Goddéris et al., 2017), promote strong chemical weathering and substantial CO_2 drawdown even under relatively modest CO_2 levels and consistent with simulated (Manabe and Bryan, 1985) latitudinal climate gradients. Therefore, mappable paleogeographic features within the equatorial belt—such as the distribution of equatorial land area or more specifically arc–continent collisions (Macdonald et al., 2019) (Fig. 1C), increased continental exposure during long-term marine regressions associated with supercontinent assembly (Zhang et al., 2025), continental arc length (Cao et al., 2017), and continental large igneous provinces (LIPs; Kent and Muttoni, 2013; Park et al., 2021) (Fig. 1D)—are critical for understanding the Phanerozoic CO_2 balance and its links to major climate events.

It is, however, already clear that inferences of global temperature from the available empirical or modeled CO_2 records (Fig. 1B) do not always have a consistent relationship to the first-order record of Phanerozoic glaciations. As expected, the LCIA is generally associated with low pCO_2 estimates, especially for the last few million years for which there are varied sources of consistent data (Fedorov et al., 2013). The LPIA and LD are also associated with low pCO_2 estimates from the empirical proxy record and GEOCARBSULF_volc, whereas the COPSE and especially SCION models are characterized by more variable and often much higher pCO_2 estimates (e.g., ~400 ppmv with COPSE versus ~4000 ppmv with SCION for LD at 350 Ma). More problematic still is that all the carbon-cycle models yield even higher pCO_2 for the Hirnantian (~450 Ma) ice age, which is characterized by unambiguous glaciation features preserved in the stratigraphic record of North and West Africa (Ghienne et al., 2023) and elsewhere in high southern paleolatitudes. Recent compilations of pCO_2 proxies hardly extend back before the Devonian or ~420 Ma (Foster et al., 2017) and thus cannot validate or refute the carbon-cycle models that tend to point to anomalously high pCO_2 levels (>2000 ppmv) in the early Paleozoic (Fig. 1B). On the other hand, all these carbon-cycle models seem to indicate relatively low pCO_2 values (<1000 ppmv), similar to those in the LPIA, from ~200 to 150 Ma within the 225 Myr-long 'Greater Mesozoic' glacial gap, although there is a paucity of pCO_2 proxy values reported for the Jurassic (Fig. 1B) (Foster et al., 2017). Discrepancies between the available pCO_2 records and continental glaciations in the Early Paleozoic and elsewhere, as had also been noted, for example, by Veizer et al. (2000), prompted Crowley and Berner (2001) to suggest the need to expand the scope of climate modeling to resolve these dilemmas. Accordingly, an important paper by Goddéris et al. (2014) increased the complexity of climate models with explicit consideration of the hydrological cycle and the role of paleogeographic factors such as the latitudinal distribution of continents to modulate climate through CO_2 consumption by silicate weathering.

Rather than delve into detailed factors, such as paleogeographically-induced changes in ocean circulation that could reorganize heat transport (e.g., Haug et al., 2004; Kennett, 1977), we build on the approach of

Goddéris et al. (2014) and Goddéris et al. (2017) and review published paleogeographic reconstructions to estimate how variations in the distribution of land masses may have influenced planetary surface albedo in modulating global climate, particularly the occurrence of glaciations. This largely follows the rationale of our analysis of surface albedo with changing land-sea distributions with paleolatitude since the mid-Cretaceous (0–120 Ma; Kent and Muttoni, 2022), which we now extend to the beginning of the Cambrian Period (540 Ma) and thus encompassing the entire Phanerozoic Eon. A focus is the first-order bias in land-sea distributions by hemisphere where systematic differences in associated surface albedo imply that clouds or some other albedo-enhancing agent acted to regulate the radiative balance between

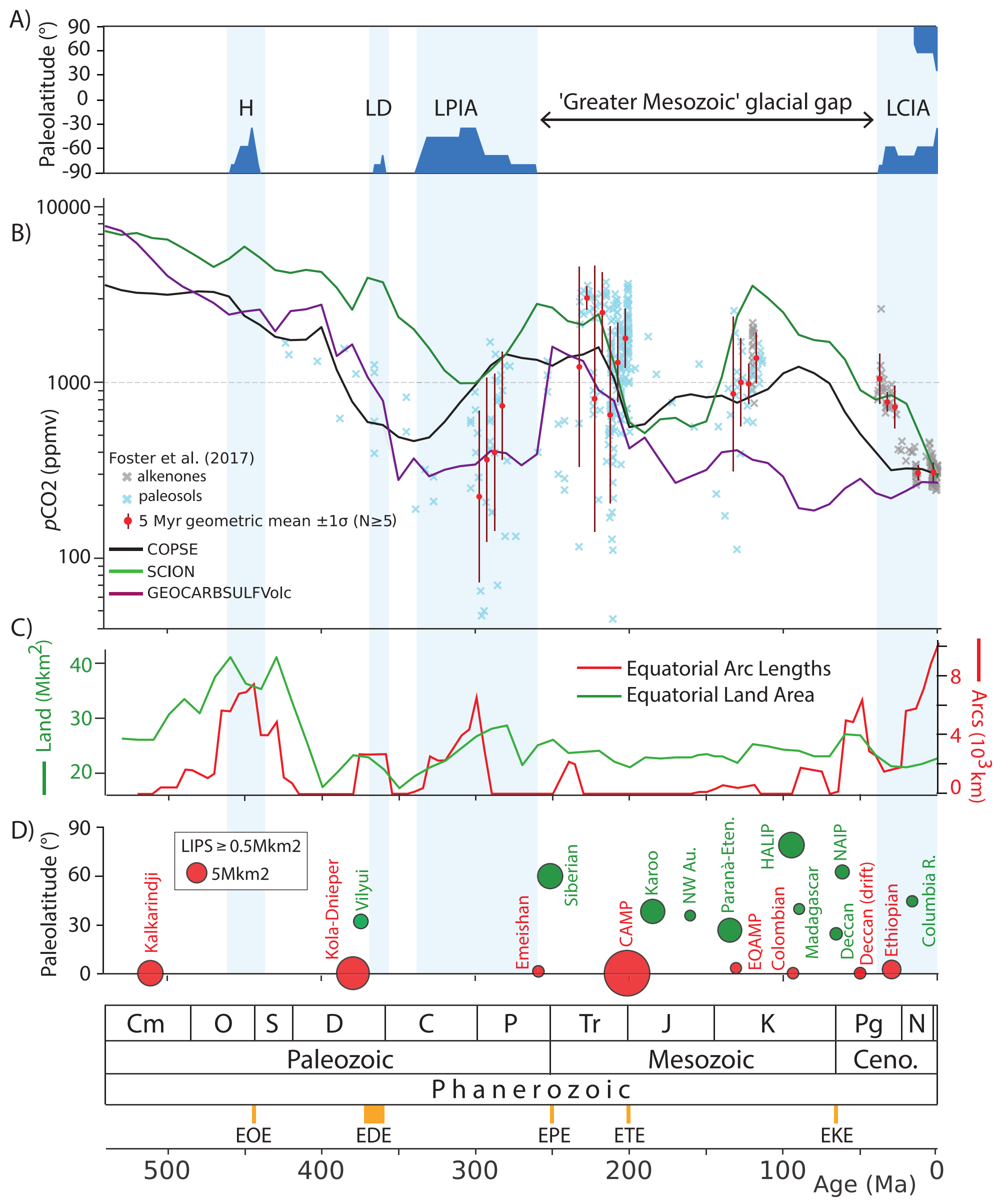

Fig. 1. (A) Plot of known Phanerozoic glaciations (H = Hirnantian, LD = Late Devonian, LPIA = Late Paleozoic Ice Age, LCIA = Late Cenozoic Ice Age) expressed as latitudinal extents of glaciations (Macdonald et al., 2019); the 'Greater Mesozoic' glacial gap is also indicated. (B) Atmospheric CO_2 concentrations through the Phanerozoic. Values for COPSE (Lenton et al., 2018), SCION (Mills et al., 2021), and GEOCARBSULF_volc (Berner, 2006a; Berner, 2006b) carbon-cycle models are taken from listings in Torsvik et al. (2024). Panel B also shows pCO_2 proxy values from paleosols and alkenones (Foster et al., 2017). This dataset was reprocessed using non-overlapping 5 Myr time bins. All CO_2 values were converted to logarithmic scale ($\log_{10} pCO_2$) to perform the averaging in multiplicative space (geometric mean). For each 5 Myr interval containing at least five independent data points ($N \geq 5$), the mean and standard deviation of $\log_{10} pCO_2$ were computed. These statistics were then back-transformed to ppmv to obtain central, lower, and upper estimates of CO_2, corresponding to the geometric mean and $\pm 1\sigma$ limits. (C) Total length of active sutures within 10° of the paleoequator (redrawn from Macdonald et al., 2019) and total area of continental land within 10° of the paleoequator (this study). (D) Latitudinal distribution of continental Large Igneous Provinces (LIPs) from Park et al. (2021). Only LIPs with areal extent $\geq 0.5 \times 10^6$ km^2 are included. Each symbol marks the paleolatitudinal position of a LIP at the time of emplacement, with symbol size proportional to its original areal extent (see Park et al., 2021). LIPs characterized by emplacement at or very close to the equator are shown in red, whereas extra-equatorial LIPs, which may nevertheless have played an important role in the broader evolution of Earth systems, are shown in green. All data are plotted with respect to the IUGS, 2024 geologic time scale (Cm = Cambrian, O = Ordovician, S = Silurian, D = Devonian, C = Carboniferous, P = Permian, Tr = Triassic, J = Jurassic, K = Cretaceous, Pg = Paleogene, Ng = Neogene, Q = Quaternary). The five major biotic mass extinctions (Sepkoski, 1996) are also shown: End-Ordovician event (EOE), End-Devonian event (EDE), End-Permian event (EPE), End-Triassic event (ETE), and end-Cretaceous event (EKE). (For interpretation of the references to colour in this figure legend, the reader is referred to the web version of this article.)

northern and southern hemispheres as shown for the present-day (Stephens et al., 2015). Although not a direct proxy for water vapor and cloudiness, we explore how estimates of hemispheric imbalance in surface albedo might provide a broad framework of long-term changes in radiative forcing of global climate to help explain how and when glaciations have occurred. A review of the time-varying distribution of land in the equatorial belt as the prime venue for CO_2 weathering sequestration complements the analysis.

2. Paleogeography and hemispheric land asymmetry

For paleogeographic reconstructions, we use apparent polar wander (APW) paths and associated plate tectonic reconstruction parameters from the literature (Besse and Courtillot, 2002; Besse and Courtillot,

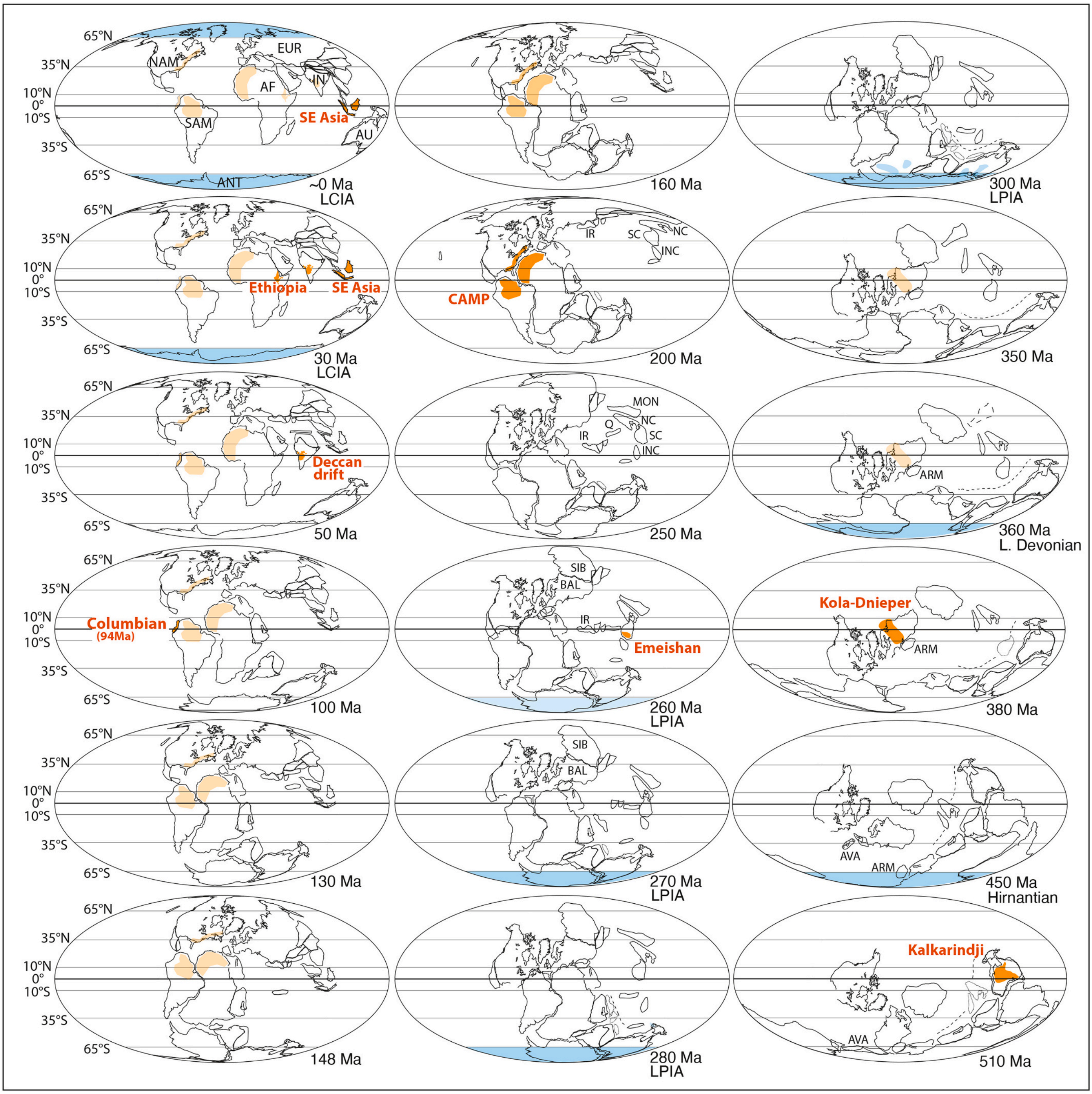

Fig. 2. Representative paleogeographic reconstructions showing the evolution of hemispheric land distributions over the Phanerozoic; the full set of 53 reconstructions is provided in Fig. SI1A–F (details in SI1; maps generated using PaleoMac, Cogné, 2003). Plate and terrane acronyms identify the main continental blocks discussed in the text: NAM, North America; SAM, South America; AF, Africa; EUR, Eurasia; ANT, Antarctica; AU, Australia; IN, India; IR, Iran; SC, South China; NC, North China; INC, Indochina; MON, Mongolia; Q, Qiangtang; ARM, Armorica; AVA, Avalonia; SIB, Siberia; BAL, Baltica. Dark orange shading denotes Large Igneous Provinces/arcs emplaced within the equatorial band, whereas light orange indicates LIPs/arcs variably persisting within the equatorial band during subsequent plate motion. The distribution of polar latitudinal belts that presumably hosted the highest concentration of ice cover during the Hirnantian, Late Devonian, LPIA, and LCIA glaciations is illustrated by blue shading. (For interpretation of the references to colour in this figure legend, the reader is referred to the web version of this article.)

2003; Kent and Irving, 2010; Torsvik et al., 2012) (see SI1). We present 53 paleogeographic reconstructions interpolated at 10-Myr intervals spanning the Phanerozoic Eon from the Early Cambrian (~530 Ma) to the present (SI1: Fig. SI1A–F), a subset of which is shown in Fig. 2. The reconstructions show the progressive assembly of Pangea during the Paleozoic Era with the convergence of Gondwana, Laurentia, Siberia, and Baltica, culminating by about 300 Ma in the Carboniferous in a Pangea B configuration (Irving, 1977; Muttoni et al., 2003; Channell et al., 2022; Kent and Muttoni, 2020). During the Permian, Pangea undergoes internal reconfiguration from Pangea B (with the northern margin of South America adjacent to the eastern margin of North America) to Pangea A (the more familiar pre-dispersal configuration with the northern margin of Africa adjacent to the eastern margin of North America) through a complex dextral shear system between Gondwana (e.g., South America and Africa) and Laurasia (e.g., North America and Europe) involving intervening crustal blocks (Irving, 2004; see also Aubele et al., 2014; Muttoni et al., 2009a). The geometry and kinematic evolution of Pangea B remain actively debated (e.g., Domeier et al., 2012 versus Kent and Muttoni, 2020). Nevertheless, even alternative global reconstructions generally imply a Carboniferous configuration broadly equivalent to Pangea B, differing mainly in the timing and kinematics of its transition toward the classic Pangea A arrangement (e.g., Torsvik et al., 2012, figs.18,19). Here we follow the paleomagnetically based reconstruction of Kent and Muttoni (2020), in which the transformation from Pangea B to Pangea A occurred during the Permian. From its formation at 260 Ma in the Late Permian to 180 Ma in the Early Jurassic, Pangea A drifted northward immediately followed by progressive fragmentation toward the current distribution of continents. The Jurassic paleogeographic reconstructions in terms of the latitudinal framework also incorporate a true polar wander episode (Kent and Irving, 2010), subsequently elaborated (Kent et al., 2015; Muttoni and Kent, 2019; Muttoni et al., 2025), which is characterized by a rapid shift with respect to the spin axis (monitored as the geocentric axial dipole from paleomagnetism) of the whole Earth including all the major tectonic plates about an equatorial Euler pivot located near present-day western Africa. In particular, the reconstruction at ~150 Ma is essentially derived from the 148 Ma cusp paleomagnetic pole of Muttoni et al. (2025), which records the acme of this global polar shift. Although the magnitude and timing, and even existence, of this Jurassic true polar wander event remain actively debated (e.g., Kulakov et al., 2021 versus Muttoni et al., 2025), the hypothesis has gained considerable attention because it provides a coherent explanation for a range of otherwise difficult-to-reconcile paleomagnetic, paleoclimatic and paleoenvironmental observations (e.g., Hou et al., 2024; Yi et al., 2019; Muttoni et al., 2025).

Within these reconstructions of the major continents, we also included, where possible, the positions of several key mobile terranes. For the Paleozoic interval, we reconstructed the northward drift of the Avalonian terranes from Gondwana, as well as the migration of the Armorican block. Our proposed reconstruction of Armorica places this block accreted against Europe in a more easterly position, adjacent to the southern margin of the East European craton (Fig. 2, reconstruction at 380 Ma), which avoids the need for an extended sinistral motion of Armorica relative to Gondwana in the mid-Paleozoic (~Devonian) as in some conventional reconstructions (e.g., Torsvik et al., 2012). This proposed geometry of accretion was subsequently modified by right-lateral shear during the Pangea B to Pangea A transition (Muttoni et al., 2009a), ultimately leading to the present longitudinal position of Armorica relative to Europe. In the Tethyan realm, the Cimmerian blocks (e.g., Iran) progressively migrated northward across the Tethys Ocean from the Early Permian to the Late Triassic (Muttoni et al., 2009b) where relative motions of the China-Indochina blocks are reconstructed essentially following Kent and Muttoni (2020) (Fig. 2). We have also positioned on these paleogeographic reconstructions several key continental Large Igneous Provinces (LIPs) emplaced in the equatorial humid belt (within ±10° paleolatitude), an optimal (warm and humid) venue for continental silicate weathering leading to carbon sequestration (Dessert et al., 2003; Kent and Muttoni, 2008; Kent and Muttoni, 2013; Macdonald et al., 2019) following Table 7.1 in Park et al. (2021) with original estimated areas in million square kilometers (Mkm^2).

Overall, these reconstructions are broadly consistent with other global compilations (e.g., Torsvik et al., 2012), especially for the past ~180 Ma when reasonably well-defined apparent polar wander paths (APWPs) as well as oceanic kinematic constraints (spreading histories, transform trends) are available. There are nonetheless different interpretations of paleogeography and plate kinematics debated already for the Jurassic, notably the True Polar Shift. For the Paleozoic, paleogeographic configurations remain even less well constrained, partly due to the lower quality of APWPs and partly because of the lack of preserved oceanic kinematics to fix relative longitudinal relationships among Laurentia, Baltica, Siberia, and Gondwana, as well as the still limited knowledge on the positions of Gondwana-related blocks. Nevertheless, for the purpose of this work—namely, the calculation of continental land distribution across climatic latitudinal belts averaged by hemisphere—such longitudinal uncertainties in Paleozoic reconstructions are not expected to have much impact. With the paleogeographic reconstructions in hand, we calculated continental (land) surface areas distributed across latitudinal belts (0–10°, 10–35°, 35–65°, 65–90° in both hemispheres), which approximate idealized climate belts (Manabe and Bryan, 1985; see also Kent and Muttoni, 2022). As digitized continental areas from paleogeographic reconstructions may carry uncertainties of a few million square kilometers, all surfaces were proportionally rescaled so that the total land area is close to a reference of 150 Mkm^2, approximating the present-day value (see SI2: Text S2 and Table S4). Even after normalization, we estimate a residual uncertainty of about ±10% relative to the 150 Mkm^2 reference value. In the absence of any observed long-term Phanerozoic trend in continental lithosphere volume, this gross estimated uncertainty reflects tectonic and glacioeustatic changes in continental outlines.

Within these uncertainties, we find that the long-term evolution of continental land distribution reveals a robust asymmetry between the northern and southern hemispheres that slowly shifted through time. During the Paleozoic, landmasses were predominantly concentrated in the Southern Hemisphere (Fig. 3A) where Gondwana dominated the globe and imposed a globally unbalanced paleogeography. The Pangea B to Pangea A reconfiguration in the late Permian (~260 Ma) marked a transition toward a more balanced hemispheric continental distribution that continued through the entire Mesozoic (252 to 66 Ma) and into the early Cenozoic with the progressive breakup of Pangea. By around 34 Ma in the Cenozoic, this trend reversed as the Atlantic widened and the bordering continents drifted farther northward. With India drifting from the Southern Hemisphere to dock with Asia during the early Paleogene, with proposed collision-onset ages ranging from the middle Paleocene (~59 Ma; Hu et al., 2015) to the early Eocene (~50–46 Ma; Najman et al., 2010; Dupont-Nivet et al., 2010), depending on the definition and criteria used to date collision, the Northern Hemisphere acquired a dominant share of land area culminating in the present-day asymmetry (Fig. 3A).

Based on these data, we computed a hemispheric land bias index (ΔH), which is the ratio of the difference in land area between the Northern Hemisphere (NH) and the Southern Hemisphere (SH) to total land area at each time step (Ma): $\Delta H = (NH - SH) / (NH + SH)$, where $NH + SH = 150$ Mkm^2. The ΔH index (Fig. 3B; Table S4), which theoretically ranges from +1 (all land in the NH) to −1 (all land in the SH), exhibits a long-term variation across the Phanerozoic. In the Paleozoic, ΔH has consistently negative values, about −0.8 in the Cambrian to Devonian (~530–350 Ma) gradually changing to about −0.2 over much of the ensuing Carboniferous and Permian interval (~350–260 Ma), reflecting a progressive shift to a more balanced interhemispheric distribution of land area. The ΔH index then stays in a relatively narrow range from −0.2 and +0.2 for the entire Mesozoic and the Cenozoic up to ~34 Ma when it gradually increases above +0.2, reflecting a more

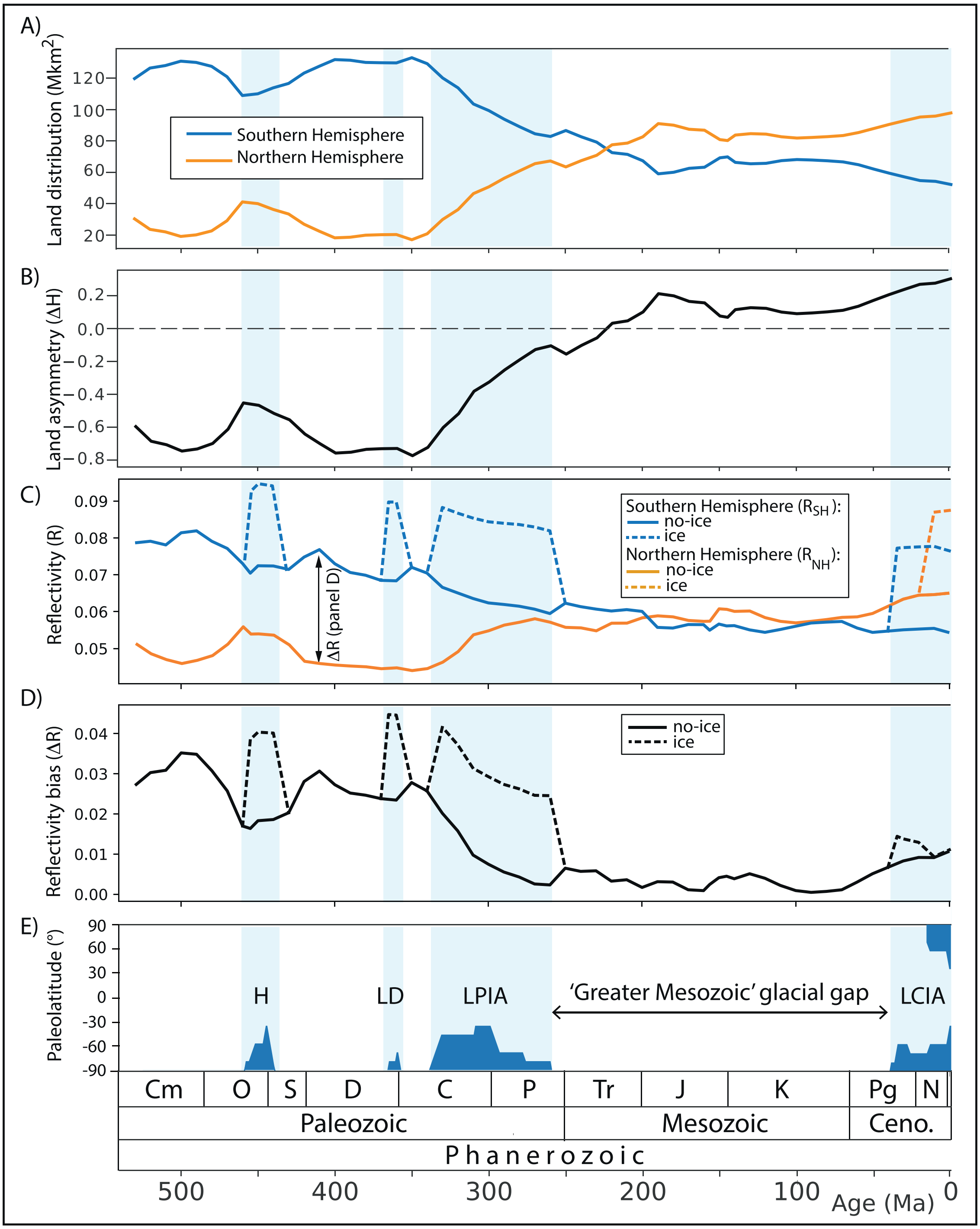

Fig. 3. (A) Land distribution (Mkm^2) through the Phanerozoic for the Southern Hemisphere and the Northern Hemisphere. (B) Land asymmetry index ΔH (dimensionless; positive values indicate a greater proportion of land in the Northern Hemisphere while negative values indicate more land in the Southern Hemisphere). (C) Reflectivities of the northern and southern hemispheres without ice (solid line) and with high latitude ice in glaciated hemisphere(s) (dashed line) variably imposed as ice albedo = 0.60 in the |65–90°| paleolatitude bands. (D) Reflectivity bias index ΔR without ice (solid line) and with polar ice in glaciated hemisphere(s) (dashed line). In panels C and D, during glacial intervals, the no-ice curves represent the corresponding paleogeographic configuration with the ice contribution removed. (E) Plot of the known Phanerozoic glaciations (H = Hirnantian, LD = Late Devonian, LPIA = Late Paleozoic Ice Age, LCIA = Late Cenozoic Ice Age) expressed as latitudinal extents of glaciations (Macdonald et al., 2019); the 'Greater Mesozoic' glacial gap is also indicated. All data are plotted with respect to the IUGS, 2024 geologic time scale (acronyms as in Fig. 1).

north-biased continental configuration up to the present. What is noteworthy is that the balanced Earth interval corresponds to the absence of evidence for glaciation from ~260 Ma to ~34 Ma, the 'Greater Mesozoic' glacial gap (Fig. 3), suggesting some connection(s) between hemispheric land distribution and global climate forcing that we explore below.

3. Interhemispheric reflectivity bias

To reconstruct Northern Hemisphere reflectivity (R_{NH}) and Southern Hemisphere reflectivity (R_{SH}) through the Phanerozoic, we first estimated area-weighted surface-reflectivity contributions for four latitudinal belts (see below), separated into land and sea components in both hemispheres, for each paleogeographic reconstruction time interval (see SI2: Text S3). Here, reflectivity refers to the area-weighted contribution of each latitudinal belt to the total planetary reflectivity. Because each contribution is normalized to the same total Earth surface area, the contributions from individual latitude bands and hemispheres can be summed to obtain hemispheric and global reflectivity (see SI2: Text S3).

The adopted values broadly follow the approximate surface-reflectivity scheme used by Kent and Muttoni (2022) for 0–120 Ma, which essentially follows Barron et al. (1980), with modifications introduced here to account for long-term terrestrial vegetation evolution. For the 0–420 Ma interval, we used the following values: tropical humid $|0–10°|$: land = 0.10, sea = 0.06; subtropical arid $|10–35°|$: land = 0.35, sea = 0.06; temperate $|35–65°|$: land = 0.15, sea = 0.10; and polar $|65–90°|$: land = 0.15, sea = 0.10. During known ice ages, polar $|65–90°|$ reflectivities are set to 0.60 for both land and sea, distinguishing between predominantly monopolar Paleozoic glaciations (H, LD, LPIA) and the initially monopolar, subsequently bipolar, Cenozoic glaciation (LCIA).

For intervals older than 420 Ma, we account for the possible effect of less developed terrestrial vegetation on continental albedo. Following the broad vegetation-evolution framework discussed by Le Hir et al. (2011; but see also Strother et al., 2015) and using representative albedo values for different land-cover types, we assign higher continental reflectivities to pre-Devonian (>420 Ma) equatorial and mid-latitude land surfaces than to their post-Devonian counterparts. Specifically, we use land reflectivities of 0.20 for the $|35–65°|$ and $|0–10°|$ belts during the Eoembryophytic phase (530–460 Ma), 0.17 and 0.15, respectively, during the Eotracheophytic phase (450–430 Ma), and 0.15 and 0.10, respectively, during the Eutracheophytic–modern phase (420–0 Ma). This vegetation correction is treated as a first-order parameterization rather than a detailed paleobotanical reconstruction, because the effective albedo contrast between unvegetated humid soils and vegetated surfaces remains uncertain and may vary with substrate, moisture, and vegetation structure.

The use of fixed latitudinal albedo belts is necessarily a first-order approximation. Regional deviations from this zonal structure may have occurred, particularly during supercontinent intervals when paleomonsoonal circulation could have modified precipitation, aridity, vegetation cover, and hence land-surface reflectivity. The Pangean megamonsoon has long been discussed as an important feature of supercontinent climate, especially for the Triassic (Parrish, 1993). However, monsoonal effects are spatially heterogeneous and seasonally variable, and no continuous quantitative reconstruction of monsoon-driven aridity exists for the full Phanerozoic at the resolution required here. Moreover, paleomagnetic inclination shallowing-corrected paleolatitudes and climate-sensitive facies from Late Triassic rift basins in the North America-Greenland-Europe sector of Pangea support a broadly zonal climatic structure, with a humid equatorial belt and more arid subtropical belts (Kent and Tauxe, 2005). We therefore retain fixed zonal albedo values as a transparent baseline while treating paleomonsoonal modulation of regional albedo as an uncertainty to be addressed by future coupled climate-model studies.

The zonal reflectivity values illustrated above were assigned to land surfaces within each latitudinal band under two scenarios. In the no-ice scenario, no glacial albedo is imposed in the polar regions, even during known ice ages, in order to isolate the paleogeographic component of reflectivity (Table S5). In the ice scenario, polar glacial albedo is implemented during recognized glacial intervals (Table S6). Outside these intervals, and for all surfaces not affected by ice, the albedo values in Table S6 are identical to those in Table S5. Then, at each time step, land and complementary sea areas within each latitudinal belt (Table S4) were assigned their respective surface reflectivities. Area-weighted reflectivity contributions were then summed across the four belts of each hemisphere and normalized to total Earth surface area, yielding Northern Hemisphere reflectivity (R_{NH}) and Southern Hemisphere reflectivity (R_{SH}) through time (SI2: Text S3), reported for the no-ice scenario (solid lines, Fig. 3C; Table S7) and for the ice scenario (dashed lines, Fig. 3C; Table S8). The absolute difference between R_{NH} and R_{SH} defines the interhemispheric reflectivity bias index, ΔR (SI2: Text S4), also reported for the no-ice scenario (Fig. 3D; Table S7) and the ice scenario (Fig. 3D; Table S8) at each time step.

4. Interhemispheric balance and global compensated reflectivity

The conceptual calculation of total reflectivity depends on whether the two hemispheres are radiatively symmetric or asymmetric. In the symmetric case, R_{NH} and R_{SH} are equal, or sufficiently balanced, and the total planetary reflectivity can be obtained by simply summing the two hemispheric contributions. This is illustrated by the simplified conceptual example in Fig. 4A, which considers an oceanic planet with a single continent symmetrically arranged with respect to the equator, without including additional atmospheric components; under these idealized symmetric conditions, total reflectivity is simply the sum of R_{NH} and R_{SH}.

The asymmetric case needs to be treated differently. Satellite data show that Earth's planetary albedo is nearly identical between hemispheres, despite the strong land–sea contrast that makes the surface of the Northern Hemisphere brighter (Datseris and Stevens, 2021; Stephens et al., 2015). This remarkable modern hemispheric symmetry in planetary albedo is thought to result from compensating processes within the coupled ocean–atmosphere system. Clouds likely play an important role although the exact mechanism remains uncertain and may involve multiple interacting factors operating across different timescales (Datseris and Stevens, 2021). In the simplified conceptual example of the asymmetric case (Fig. 4B), the land-dominated hemisphere is more reflective whereas the other hemisphere is ocean-dominated and more absorbing, and therefore warmer. In this condition, the two hemispheric reflectivities cannot be treated as radiatively balanced without an additional compensating term. The imbalance is expressed as ΔR, defined above as the absolute reflectivity difference between the two hemispheres. Here, compensation is represented by adding reflective cloud cover over the warmer, less reflective hemisphere until its reflectivity matches that of the cooler, more reflective hemisphere (Fig. 4C). Once this balance is restored, the global compensated reflectivity (GCR) can be calculated, representing a hypothetical fully compensated interhemispheric state where differences in surface reflectivity between the hemispheres are compensated by combining the estimated surface reflectivities of both hemispheres and adding their absolute difference (ΔR) at each time step: $GCR = R_{NH} + R_{SH} + \Delta R$ (SI2: Text S5).

Interhemispheric compensation could, in principle, be achieved through geological, biological, or physical mechanisms other than increased cloud cover over the darker, warmer hemisphere. For example, one could envisage the opposite mechanism, in which the brighter, colder hemisphere is darkened by volcanic dust, mineral dust, black carbon, wildfire-derived soot, or other surface-darkening processes, including the expansion of vegetation cover. Such processes are physically plausible: wildfire-derived light-absorbing impurities can reduce snow and ice albedo and enhance surface energy absorption, although wildfire smoke in the atmosphere may also reduce incoming shortwave radiation and partly offset the melt-enhancing effect of surface darkening (Aubry-Wake et al., 2022). However, darkening mechanisms appear less suitable as a general, continuously operating compensation process over geological time: dust and volcanic forcing

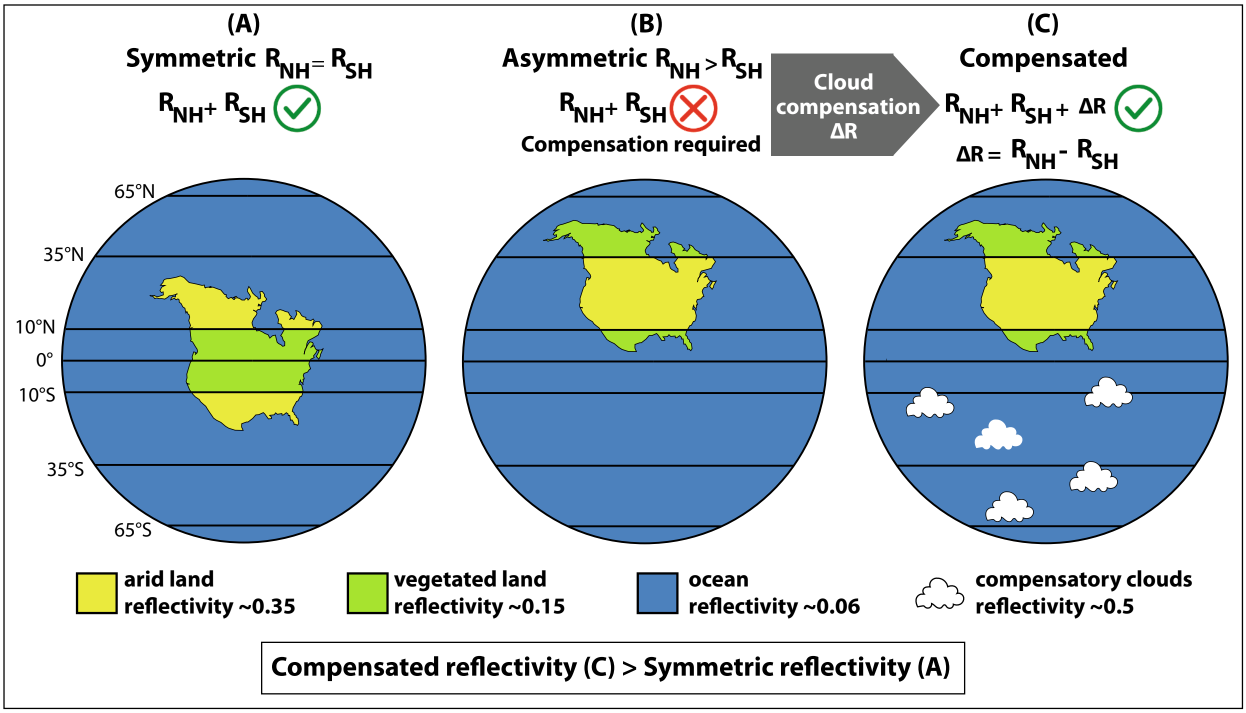

Fig. 4. Conceptual model of hemispheric reflectivity compensation. (A) Symmetric configuration, in which Northern and Southern Hemisphere reflectivities (R_{NH} and R_{SH}, respectively) are balanced and total reflectivity is simply their sum. (B) Asymmetric configuration, in which one hemisphere is more reflective and the other more absorbing, generating an interhemispheric reflectivity bias ΔR. (C) Compensated configuration, in which additional reflectivity, illustrated here as cloud cover over the warmer hemisphere, balances the two hemispheres and increases total reflectivity by ΔR.

are commonly episodic, mineral dust can be scattering as well as absorbing, black-carbon or soot effects are most effective on snow and ice surfaces, and vegetation shifts are spatially and biologically constrained. If a persistent darkening regime had dominated in the past, compensation would have been achieved in a fundamentally different energetic state, by lowering the reflectivity of the brighter hemisphere rather than by increasing the reflectivity of the darker one. At present, however, we are not aware of a mechanism capable of producing such systematic darkening continuously at hemispheric scale through the Phanerozoic. On the other hand, greater evaporation could be expected in the darker, more oceanic hemisphere and result in preferentially more clouds in that hemisphere. Given that strongly asymmetric land–sea configurations are common through much of the analyzed geological record, compensatory cloud development, following the modern analogue of hemispheric albedo symmetry (Stephens et al., 2015; Datseris and Stevens, 2021), appears to represent the most flexible and observationally supported mechanism, although its detailed physical implementation in deep time remains to be investigated.

An alternative mechanism proposed in the climate literature is that hemispheric radiative asymmetries may be compensated, at least in part, by cross-equatorial heat transport associated with shifts of the Intertropical Convergence Zone (ITCZ), rather than by albedo compensation alone (e.g., Chiang and Bitz, 2005; Siler et al., 2018; Laguë et al., 2021). However, present-day observations indicate that the annual-mean cross-equatorial atmospheric heat transport is directed from the NH toward the SH (Donohoe et al., 2013), despite the SH having a lower surface albedo that is largely offset at the planetary scale by enhanced cloud reflectivity (Stephens et al., 2015; Datseris and Stevens, 2021). We therefore adopt the cloud-compensated GCR framework as a working hypothesis, while recognizing that the relative contributions of cloud compensation and cross-equatorial heat transport in maintaining hemispheric energy balance remain to be quantified. Here we therefore implement interhemispheric compensation by adding clouds, with an assumed average albedo of 0.50, over the darker hemisphere to balance hemispheric reflectivities (Datseris and Stevens, 2021) (Fig. 4C). In contrast, simply summing the surface reflectivities of both hemispheres, as in Kent and Muttoni (2022), does not resolve the interhemispheric imbalance and produces a more subdued global surface-albedo profile through time. GCR values were calculated for both the no-ice scenario, in which no glacial albedo is imposed during known glacial intervals in order to isolate the background paleogeographic reflectivity signal (Fig. 5A, solid line; Table S7), and the more realistic ice scenario, in which compensated reflectivity includes the dominant effect of polar ice albedo during glacial periods (Fig. 5A, dashed lines; Table S8). GCR values for the no-ice scenario are relatively high in the Paleozoic and decrease through time toward a broad minimum during the 'Greater Mesozoic' glacial gap with the absolute minimum below 0.12 at ~100 Ma, and then slightly rise again during the ensuing part of the Cenozoic (Fig. 5A). In the ice scenario, GCR values are ~0.17 or higher during glacial intervals as a result of the strong polar ice-albedo contribution (Fig. 5A).

In all these cases, compensation is modeled by adding clouds uniformly over the darker, warmer hemisphere at each time step. Our modeling indicates that counterbalancing the large Southern Hemisphere land bias during the Paleozoic would require compensation by up to ~10–15% of extra cloud fraction in absence of ice and up to ~20% during the Paleozoic ice ages (SI2: Text S6 and Fig. S2). If the compensating clouds were to be concentrated over specific target latitude bands (e.g., |35°–65°|), the required fraction there can be much higher, e.g., ~40–50% but less than the physical limit of 100% for that band. We emphasize that the difference between the cloud-compensated GCR values and the total all-sky planetary albedo, for example ~0.3 today, is interpreted here as residual atmospheric reflectivity not directly involved in the compensating mechanism and is therefore not modeled in this study.

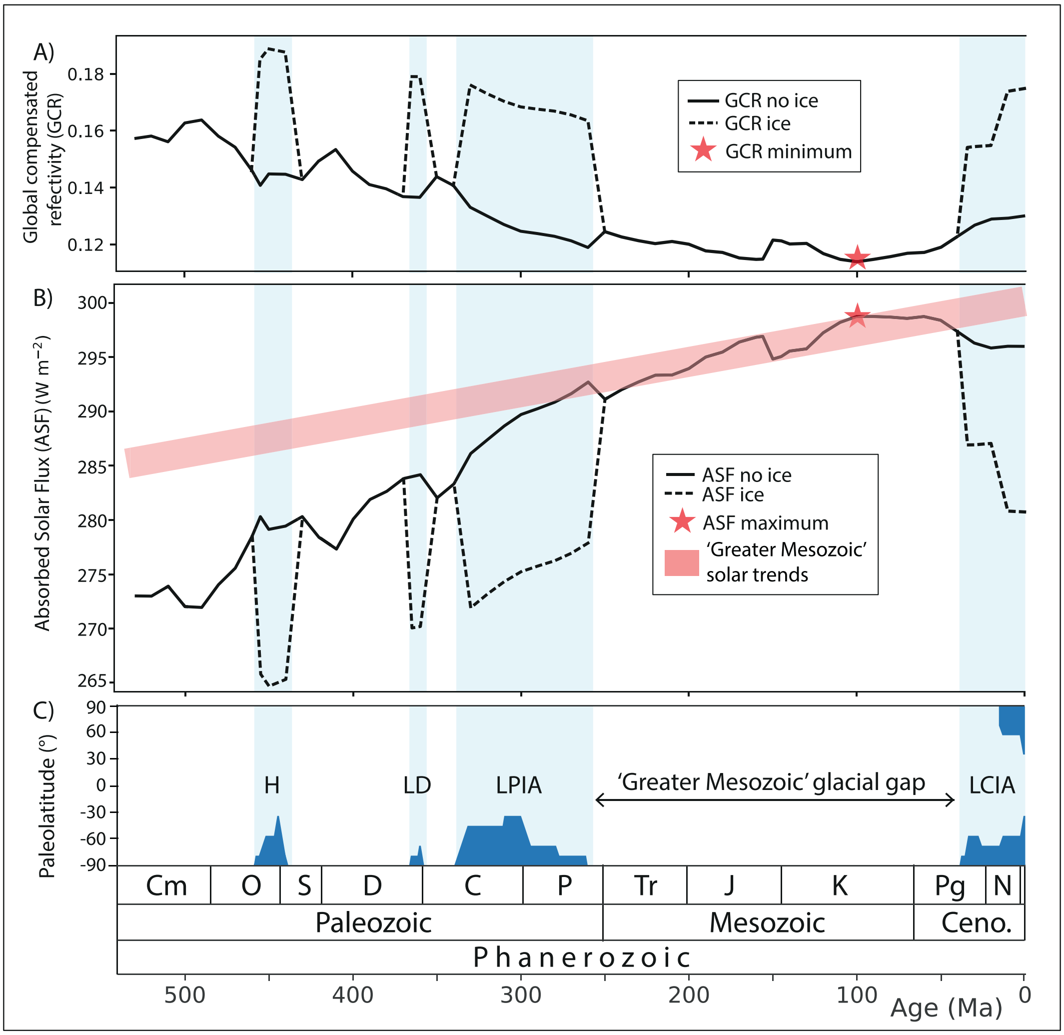

Fig. 5. (A) Global compensated reflectivity (GCR) without polar ice (solid line) and with polar ice in glaciated hemisphere(s) (dashed line). (B) Absorbed Solar Flux (ASF) without polar ice (solid line) and with polar ice in glaciated hemisphere(s) (dashed line). In panels A and B, during glacial intervals, the no-ice curves represent the corresponding paleogeographic configuration with the ice contribution removed. The light red shading in panel B represents a family of possible solar-evolution trends anchored to GCR values typical of the 'Greater Mesozoic' glacial gap; the red star at 100 Ma in panel (A) marks one such GCR value—the minimum in the record—corresponding to the maximum ASF value in panel (B). (C) Plot of the known Phanerozoic glaciations (H = Hirnantian, LD = Late Devonian, LPIA = Late Paleozoic Ice Age, LCIA = Late Cenozoic Ice Age) expressed as latitudinal extents of glaciations (Macdonald et al., 2019); the 'Greater Mesozoic' glacial gap is also indicated. All data are plotted with respect to the IUGS, 2024 geologic time scale (acronyms as in Fig. 1). (For interpretation of the references to colour in this figure legend, the reader is referred to the web version of this article.)

5. Absorbed solar flux

Building on GCR, we can further estimate the absorbed solar flux (ASF), defined here as the globally averaged shortwave energy absorbed by the Earth after accounting for both secular solar evolution and the paleogeography-controlled, compensated surface reflectivity (GCR) (SI2: Text S7). We compute the time-dependent solar input at the top of the atmosphere from the solar constant S_0, scaled for long-term stellar evolution. For the Phanerozoic interval considered here, a linear approximation of ~1% decrease in solar luminosity per 110 Myr backward in time, and corresponding brightening forward in time, is sufficiently accurate, while for older intervals and longer timescales, the formulation of Gough (1981) provides a more physically based albeit non-linear description of solar evolution. This becomes especially important for the Precambrian, where the weaker young Sun (Feulner, 2012) represents a major boundary condition for testing deep-time climate states, including Snowball Earth scenarios.

Thus, in this study we use a present-day solar constant $S_0 \approx 1361$ W m^{-2}, decreased backward in time by 1%/110 Myr. To account for Earth's spherical geometry and rotation, the effective solar flux is expressed as $S_0/4$, which represents the globally averaged incoming solar flux over a rotating spherical Earth; at present, this corresponds to approximately 340 W m^{-2}. The time-dependent absorbed solar flux (ASF) is then obtained by subtracting the compensated reflectivity contribution, expressed by GCR, from the incoming solar flux: ASF = [1 − GCR] * [S_0/4], expressed in W m^{-2}. ASF is evaluated consistently for both the no-ice scenario (Table S7) and ice scenario (Table S8), thereby capturing the combined imprint of long-term solar evolution and paleogeographic change through GCR (Fig. 5B). This provides an energetic baseline for evaluating the radiative preconditions associated with Paleozoic and Late Cenozoic ice ages.

6. Energetic boundary conditions for Phanerozoic climate

The ASF curve in the no-ice scenario, in which no prescribed glacial albedo is imposed even during known glacial intervals, shows a broad decrease backward in time. Paleozoic ASF values are several W m^{-2} lower than Mesozoic–Cenozoic values, locally by up to ~15 W m^{-2}

(Fig. 5B; Table S7). This long-term decrease primarily reflects the lower solar luminosity in the past, but the curve is clearly not a simple linear solar trend. Instead, it is strongly modulated by paleogeography through changes in GCR, producing deviations of several W m^{-2} from a purely solar evolution. Because Fig. 5B shows ASF and not incoming solar flux alone, any reference solar trend must be anchored to an assumed GCR state rather than drawn directly from the present-day $S_o/4$ value (~340 W m^{-2}).

Among the various possible anchor points, we chose the range of GCR values characteristic of the 'Greater Mesozoic' glacial gap to define a family or band of linear solar-evolution trends (Fig. 5B, light red shading). During this ~225 Myr-long interval, from the LPIA exit at ~260 Ma to the LCIA onset at ~34 Ma, land distribution was characterized by relatively high interhemispheric symmetry and the system remained radiatively balanced under generally ice-free, warm conditions, reaching a Phanerozoic ASF maximum around 100 Ma (Fig. 5B, red star). Although transient cold snaps may have occurred during the 'Greater Mesozoic' glacial gap, they did not develop into a sustained ice-mode state (Royer et al., 2004). This interval therefore provides a useful greenhouse reference against which the lower-ASF preconditions of Paleozoic and Late Cenozoic glaciations can be evaluated.

Inspection of Fig. 5B shows that the conditions immediately preceding the onset of the Paleozoic glaciations – H, LD and LPIA – occur at relatively low no-ice ASF values, approximately within the 278–283 W m^{-2} range. These values lie well below the solar-evolution reference envelope calibrated to the 'Greater Mesozoic' glacial gap greenhouse interval. A similar, although weaker, pattern is observed before the LCIA: from the ASF climax at 100 Ma to around 40 Ma, shortly before the onset of major Antarctic glaciation at ~34 Ma, ASF follows a slight downward trend and falls modestly below the 'Greater Mesozoic' reference solar trend. When polar ice albedo is imposed during recognized Paleozoic and Late Cenozoic glacial intervals, the ice-scenario ASF curve drops sharply, locally by several W m^{-2} to more than 10 W m^{-2}, reflecting the strong impact of polar ice-albedo feedback on the absorbed shortwave energy budget during glacial bifurcation (Fig. 5B).

These lower-energy states should not be interpreted as direct causes of glaciation. Rather, lower ASF establishes a lower-energy climatic background that may increase the susceptibility of the Earth system to glaciation, provided that coupled carbon-cycle feedbacks do not fully compensate the radiative deficit (Walker et al., 1981). However, relative to the 'Greater Mesozoic' greenhouse reference trend, Paleozoic glacial intervals occurred under markedly reduced energetic preconditions, reflecting paleogeographic ASF modulation associated with strongly asymmetric land–sea configurations, extensive Southern Hemisphere continentality, and a more oceanic Northern Hemisphere requiring compensatory reflectivity, represented here by additional cloud cover. Other mechanisms, such as changes in atmospheric pCO_2, may then act upon these different energetic backgrounds. In this sense, because Paleozoic glaciations initiated under lower-ASF preconditions, they may have crossed the glacial bifurcation threshold at different, possibly higher, pCO_2 levels than the LCIA onset, which developed under comparatively higher ASF conditions. In this view, ASF does not trigger glaciation directly, but may modulate the pCO_2 threshold at which glacial onset becomes possible, a hypothesis that should be tested with dedicated coupled climate models.

Coupling between pCO_2 drawdown and energetic preconditions is illustrated by the Carboniferous–Early Permian. This is when paleogeography was characterized by extensive equatorial continental crust (Fig. 1C) within a Pangea B configuration (Fig. 2), favoring intense chemical weathering and low pCO_2 levels that may have helped trigger and sustain the LPIA, together with carbon sequestration in widespread coal deposits (Kent and Muttoni, 2020) and CO_2 drawdown along extensive equatorial magmatic arcs (Macdonald et al., 2019) (Fig. 1C). During the Middle Permian transition toward Pangea A, equatorial continental area decreased substantially, weakening the global weathering sink and allowing atmospheric CO_2 to rise, thereby contributing to Middle–Late Permian warming and deglaciation (Kent and Muttoni, 2020). In this framework, reduced ASF values in a highly asymmetric Carboniferous world may have acted as an energetic precondition that modulated the pCO_2 threshold for LPIA onset, whereas its demise was favored by the shift toward a more balanced interhemispheric land configuration, reduced paleogeography-controlled albedo asymmetry, lower concentration of land in the equatorial prime weathering belt, and higher ASF values.

Similarly, the LCIA onset can be viewed as the outcome of a long-term CO_2 drawdown plausibly initiated by enhanced silicate weathering during the northward equatorial transit of the Deccan Traps around ~50 Ma (Kent and Muttoni, 2008). This is coincident with the onset of Eocene cooling and sustained by subsequent low-latitude arc-related weathering as the extruded SE Asian volcanic arc approached/entered equatorial latitudes (Kent and Muttoni, 2013), although the magnitude and continuity of the inferred CO_2 decline remain difficult to constrain (Foster et al., 2017). This mechanism acted together with a (moderate) decline of ASF due to India providing more land area to the northern hemisphere, before the threshold-like transition into LCIA. Hence the pCO_2 threshold for LCIA onset need not have been the same as that for the LPIA because the two glaciations developed under different ASF precondition states (Fig. 5B).

The Hirnantian event warrants specific consideration because most carbon-cycle models yield extremely high pCO_2 estimates for the Late Ordovician (Fig. 1B), which seem inconsistent with the geological and climatic evidence for glaciation. We note that the Ordovician Period had exceptionally high concentrations of equatorial land in conjunction with magmatic arc exposures (Fig. 1C), which should have drawn down atmospheric CO_2—potentially toward a threshold comparable to LPIA onset, given the similar background ASF discussed above–but which is not captured by carbon-cycle models to account for the strong silicate weathering feedback imposed by the paleogeographic configuration of that time.

7. Discussion and conclusions

Phanerozoic glaciations were infrequent, occurring only three times in the Paleozoic (H, LD, LPIA) and once in the Cenozoic (LCIA). Paleozoic glaciations in particular are associated with high GCR and low ASF states, linked to interhemispheric land biases exceeding ~20%. Conversely, low GCR and high ASF characterize the ~225 Myr-long 'Greater Mesozoic' glacial gap, an extended interval of comparatively balanced interhemispheric land distribution during which sustained glaciation was inhibited even in the presence of extreme volcanic or impact events. A particularly instructive case is the absence of sustained glaciation following emplacement of the ~201 Ma CAMP, perhaps the largest continental LIP by footprint at ~10 Mkm^2 and one that straddled the paleoequator (Figs. 1, 2), suggesting that pCO_2 forcing alone is insufficient to explain glacial inception without the appropriate paleogeographic–radiative boundary conditions.

The not always satisfactory correspondence between modeled pCO_2 and glaciations under outgassing-controlled carbon-cycle models (Fig. 1A,B) suggests that glacial initiation was governed primarily by tectonic modulation of CO_2 sinks rather than volcanic sources, within a complex interplay of feedbacks and forcings that included pCO_2 thresholds (DeConto and Pollard, 2003), orbital variations (Hays et al., 1976), and dynamic oceanic heat transport (Haug et al., 2004; Kennett, 1977). No significant correlation between LIP emplacement (Fig. 1D) and glacial timing was found by Park et al. (2021), who suggested that most continental flood basalts, especially rifting-related low elevation LIPs, acted as short-lived secondary modulators of atmospheric CO_2 rather than primary drivers of long-term sequestration. An exception may be the Deccan Traps, whose plume-derived, topographically elevated exposure could have contributed to the cooling around 50 Ma (Kent and Muttoni, 2008, 2013) and whose equator-crossing was instrumental in the inauguration of our current Northern Hemisphere land bias. On the other hand, higher concentrations of magmatic arcs—tectonically active, mafic, high-runoff orogenic belts–within equatorial landmasses (Fig. 1C) were identified by Macdonald et al. (2019) as a key first-order control on long-term CO_2 drawdown that established conditions favorable for glaciation.

Our analysis of compensated reflectivity, representing the potential of the land–sea system to modulate planetary reflectivity through time, suggests that long-term variations in ASF influenced the energetic background against which CO_2 perturbations operated. For example, the ASF contrast between 340 Ma, before LPIA onset, and 40 Ma, before LCIA onset, is ~14 W m^{-2} (Fig. 5B), reflecting both the slightly fainter Sun and the higher compensated reflectivity of Late Paleozoic Earth. Even if the surface contribution to total planetary albedo is attenuated by the atmosphere by a factor of approximately three, as suggested by modern observations (Donohoe and Battisti, 2011), the resulting ASF difference from 340 Ma to 40 Ma remains several W m^{-2}, comparable to the radiative forcing associated with CO_2 doubling (Myhre et al., 1998). This indicates that paleogeographic and solar differences can generate climatically significant radiative anomalies over multimillion-year timescales. In this framework, glaciations may have initiated when high-GCR/low-ASF states coincided with efficient CO_2 sinks, especially equatorial landmasses and orogens promoting silicate weathering and carbon burial. Phanerozoic climate susceptibility therefore depended not on CO_2 alone, but on the combined paleogeographic control of radiative symmetry, absorbed solar energy, and CO_2 sequestration efficiency.

Finally, it is interesting to note that of the Big Five mass extinctions (Raup, 1986; Sepkoski, 1996), the three most recent and best documented (66 Ma end-Cretaceous, 201 Ma end-Triassic, 252 Ma end-Permian) occur during the 225-Myr-long 'Greater Mesozoic' glacial gap (Fig. 1). Each mass extinction does coincide with a LIP (Deccan, CAMP and Siberian traps, respectively), suggesting some kind of associated forcing such as volcanic CO_2-induced hyperthermals or ocean acidification (Courtillot and Renne, 2003; Rampino et al., 2024), or repeated volcanic winters (e.g., Kent et al., 2024). Nonetheless, major glaciations were not induced even by CAMP nor by the huge Chicxulub impact with a 180 km diameter crater and the proximal cause of the end-Cretaceous mass extinction (Alvarez et al., 1980; Schulte et al., 2010) that occurred during the eruption of the Deccan Traps (Schoene et al., 2019; Sprain et al., 2019). This indicates that the low GCR characterizing the latest Paleozoic to early Cenozoic interval of equable climate was sufficient to squelch glaciations despite strong potential triggers. In contrast, the end-Ordovician and Late Devonian mass extinction events temporally coincide with the H and LD glaciations that were able to occur when the Earth system was more susceptible to ice ages because of pronounced interhemispheric land asymmetry, even in the possible presence of high pCO_2. And yet the LPIA–the longest glaciation in the Phanerozoic–was not associated with a major biotic extinction event. Mass extinctions in the Phanerozoic evidently did not have a principal causative environmental factor in common.

Declaration of competing interest

The authors declare that they have no known competing financial interests or personal relationships that could have appeared to influence the work reported in this paper.

Acknowledgements

We sincerely thank the Editor for handling this manuscript and the reviewers for their careful reading and constructive comments, which motivated us to strengthen the paper and improve its clarity. Calculations derived from the formulas described in Supplementary Information 2 were assisted by AI-based tools verified by the authors. GM acknowledges institutional support from the Department of Earth Sciences, University of Milan, through the 2023–2027 Department of Excellence program. DVK acknowledges long-standing support for this research from the Rutgers Board of Governors Research Fund and the Lamont Paleomagnetic Research Fund.

Appendix A. Supplementary data

Supplementary data to this article can be found online at https://doi.org/10.1016/j.earscirev.2026.105632.

Data availability

Data will be made available on request.

References

Alvarez, L.W., Alvarez, W., Asaro, F., Michel, H.V., 1980. Extraterrestrial cause for the Cretaceous-Tertiary extinction. Science 208, 1095–1108.
Aubele, K., Bachtadse, V., Muttoni, G., Ronchi, A., 2014. Paleomagnetic data from Late Paleozoic dykes of Sardinia: evidence for block rotations and implications for the intra-Pangea megashear system. Geochem. Geophys. Geosyst. 15 (5), 1684–1697.
Aubry-Wake, C., Bertoncini, A., Pomeroy, J.W., 2022. Fire and ice: the impact of wildfire-affected albedo and irradiance on glacier melt. Earth's Future 10, e2022EF002685. https://doi.org/10.1029/2022EF002685.
Barron, E.J., Sloan, J.L., Harrison, C.G.A., 1980. Potential significance of land—sea distribution and surface albedo variations as a climatic forcing factor; 180 m.y. to the present. Palaeogeogr. Palaeoclimatol. Palaeoecol. 30, 17–40.
Bergmann, K.D., Macdonald, F.A., Swanson-Hysell, N.L., 2025. The causes and consequences of Ordovician cooling. Annu. Rev. Earth Planet. Sci. 53, 25.1–25.35.
Berner, R.A., 1990. Atmospheric carbon dioxide levels over Phanerozoic time. Science 249, 1382–1386.
Berner, R.A., 2003. The long-term carbon cycle, fossil fuels and atmospheric composition. Nature 426 (6964), 323–326.
Berner, R.A., 2006a. GEOCARBSULF: a combined model for Phanerozoic atmospheric O2 and CO2. Geochim. Cosmochim. Acta 70 (23), 5653–5664.
Berner, R.A., 2006b. Inclusion of the weathering of volcanic rocks in the GEOCARBSULF Model. Am. J. Sci. 306, 295–302.
Besse, J., Courtillot, V., 2002. Apparent and true polar wander and the geometry of the geomagnetic field over the last 200 Myr. J. Geophys. Res. 107, 2300. https://doi.org/10.1029/2000JB000050.
Besse, J., Courtillot, V., 2003. Correction to "Apparent and true polar wander and the geometry of the geomagnetic field over the last 200 Myr". J. Geophys. Res. 108, 2469. https://doi.org/10.1029/2003JB002684.
Cao, W., Lee, C.-T.A., Lackey, J.S., 2017. Episodic nature of continental arc activity since 750 Ma: a global compilation. Earth Planet. Sci. Lett. 461, 85–95.
CENCO2PIP_Consortium, 2023. Toward a Cenozoic history of atmospheric CO2. Science 382 (6675), eadi5177.
Channell, J.E.T., Muttoni, G., Kent, D.V., 2022. Adria in Mediterranean paleogeography, the origin of the Ionian Sea, and Permo-Triassic configurations of Pangea. Earth Sci. Rev. 230, 104045. https://doi.org/10.1016/j.earscirev.2022.104045.
Chiang, J.C.H., Bitz, C.M., 2005. Influence of high latitude ice cover on the marine Intertropical Convergence Zone. Clim. Dyn. 25, 477–496. https://doi.org/10.1007/s00382-005-0040-5.
Cogné, J.P., 2003. PaleoMac: a Macintosh™ application for treating paleomagnetic data and making plate reconstructions. Geochem. Geophys. Geosyst. 4, 1007. https://doi.org/10.1029/2001GC000227.
Courtillot, V.E., Renne, P.R., 2003. On the ages of flood basalt events. Compt. Rendus Geosci. 335, 113–140.
Crowley, T.J., Berner, R.A., 2001. CO2 and climate change. Science 292 (5518), 870–872.
Datseris, G., Stevens, B., 2021. Earth's albedo and its symmetry. AGU Adv. 2 (3), e2021AV000440.
DeConto, R.M., Pollard, D., 2003. Rapid Cenozoic glaciation of Antarctica induced by declining atmospheric CO2. Nature 421, 245–249.
Dessert, C., Dupré, B., Gaillardet, J., Francois, L., Allègre, C., 2003. Basalt weathering laws and the impact of basalt weathering on the global carbon cycle. Chem. Geol. 202, 257–273.
Domeier, M., Van der Voo, R., Torsvik, T.H., 2012. Paleomagnetism and Pangea: the road to reconciliation. Tectonophysics 514–517, 14–43. https://doi.org/10.1016/j.tecto.2011.10.021.
Donohoe, A., Battisti, D.S., 2011. Atmospheric and surface contributions to planetary albedo. J. Clim. 24 (16), 4402–4418.
Donohoe, A., Marshall, J., Ferreira, D., McGee, D., 2013. The relationship between ITCZ location and cross-equatorial atmospheric heat transport: from the seasonal cycle to the Last Glacial Maximum. J. Clim. 26, 3597–3618. https://doi.org/10.1175/JCLI-D-12-00467.1.
Dupont-Nivet, G., Lippert, P.C., Van Hinsbergen, D.J.J., Meijers, M.J.M., Kapp, P., 2010. Palaeolatitude and age of the Indo–Asia collision: palaeomagnetic constraints. Geophys. J. Int. 182 (3), 1189–1198.
Eldrett, J.S., Harding, I.C., Wilson, P.A., Butler, E., Roberts, A.P., 2007. Continental ice in Greenland during the Eocene and Oligocene. Nature 446 (7132), 176–179.
Fedorov, A.V., Brierley, C.M., Lawrence, K.T., Liu, Z., Dekens, P.S., Ravelo, A.C., 2013. Patterns and mechanisms of early Pliocene warmth. Nature 496 (7443), 43–49.

Feulner, G., 2012. The faint young Sun problem. Rev. Geophys. 50. https://doi.org/10.1029/2011RG000375.
Foster, G.L., Royer, D.L., Lunt, D.J., 2017. Future climate forcing potentially without precedent in the last 420 million years. Nat. Commun. 8, 14845.
Gaffin, S., 1987. Ridge volume dependence on seafloor generation rate and inversion using long term sealevel change. Am. J. Sci. 287, 596–611.
Ghienne, J.-F., Abdallah, H., Deschamps, R., Guiraud, M., Gutiérrez-Marco Juan, C., Konaté, M., Meinhold, G., Moussa, A., Rubino, J.-L., 2023. The Ordovician record of North and West Africa: unravelling sea-level variations, Gondwana tectonics, and the glacial impact. Geol. Soc. Lond. Spec. Publ. 533 (1), 199–252.
Goddéris, Y., Donnadieu, Y., Hir, G.L., Lefebvre, V., Nardin, E., 2014. The role of palaeogeography in the Phanerozoic history of atmospheric CO2 and climate. Earth Sci. Rev. 128, 122–138.
Goddéris, Y., Donnadieu, Y., Carretier, S., Aretz, M., Dera, G., Macouin, M., Regard, V., 2017. Onset and ending of the late Palaeozoic ice age triggered by tectonically paced rock weathering. Nat. Geosci. 10 (5), 382–386.
Gough, D.O., 1981. Solar interior structure and luminosity variations. Sol. Phys. 74, 21–34.
Haug, G.H., Tiedermann, R., Keigwin, L.D., 2004. How the Isthmus of Panama put ice in the Arctic. Oceanus 42, 4 pages.
Hays, J.D., Imbrie, J., Shackleton, N.J., 1976. Variations in the Earth's orbit: pacemaker of the Ice Ages. Science 194, 1121–1132.
Hou, Y., Zhao, P., Qin, H., Mitchell, R.N., Li, Q., Hao, W., Zhang, M., Ward, P.D., Yuan, J., Deng, C., Zhu, R., 2024. Completing the loop of the Late Jurassic–Early Cretaceous true polar wander event. Nat. Commun. 15 (1), 2183.
Hu, X., Garzanti, E., Moore, T., Raffi, I., 2015. Direct stratigraphic dating of India–Asia collision onset at the Selandian (middle Paleocene, 59 ± 1 Ma). Geology 43, 859–862. https://doi.org/10.1130/G36872.1.
Irving, E., 1977. Drift of the major continental blocks since the Devonian. Nature 270, 304–309.
Irving, E., 2004. The case for Pangea B, and the intra-Pangean megashear. In: Channell, J.E.T., Kent, D.V., Lowrie, W., Meert, J.G. (Eds.), Timescales of the Paleomagnetic Field, Geophysical Monograph, 145. American Geophysical Union, Washington, D.C., pp. 13–27
IUGS, 2024. International Chronostratigraphic Chart. ChronostratChart2023-04.pdf (Editor).
Kennett, J.P., 1977. Cenozoic evolution of Antarctic glaciation, the circum-antarctic ocean and their impact on global paleoceanography. J. Geophys. Res. 82, 3843–3860.
Kent, D.V., Irving, E., 2010. Influence of inclination error in sedimentary rocks on the Triassic and Jurassic apparent polar wander path for North America and implications for Cordilleran tectonics. J. Geophys. Res. 115, B10103. https://doi.org/10.1029/2009JB007205.
Kent, D.V., Muttoni, G., 2008. Equatorial convergence of India and early Cenozoic climate trends. Proc. Natl. Acad. Sci. 105, 16065–16070.
Kent, D.V., Muttoni, G., 2013. Modulation of Late Cretaceous and Cenozoic climate by variable drawdown of atmospheric pCO2 from weathering of basaltic provinces on continents drifting through the equatorial humid belt. Clim. Past 9, 525–546.
Kent, D.V., Muttoni, G., 2020. Pangea B and the Late Paleozoic Ice Age. Paleogeogr. Paleoclimatol. Paleoecol. 553, 1–20.
Kent, D.V., Muttoni, G., 2022. Latitudinal land–sea distributions and global surface albedo since the cretaceous. Palaeogeogr. Palaeoclimatol. Palaeoecol. 585, 110718.
Kent, D.V., Tauxe, L., 2005. Corrected Late Triassic latitudes for continents adjacent to the North Atlantic. Science 307, 240–244. https://doi.org/10.1126/science.1105826.
Kent, D.V., Kjarsgaard, B.A., Gee, J.S., Muttoni, G., Heaman, L.M., 2015. Tracking the Late Jurassic Apparent (or True) Polar Shift in U-Pb dated Kimberlites from Cratonic North America (Superior Province of Canada). Geochem. Geophys. Geosyst. 16 (4), 983–994.
Kent, D.V., Olsen, P.E., Wang, H., Schaller, M.F., Et-Touhami, M., 2024. Correlation of sub-centennial-scale pulses of initial Central Atlantic Magmatic Province lavas and the end-Triassic extinctions. Proc. Natl. Acad. Sci. 121 (46), e2415486121. https://doi.org/10.1073/pnas.2415486121.
Kulakov, E.V., Torsvik, T.H., Doubrovine, P.V., Slagstad, T., Ganerød, M., Silkoset, P., Werner, S.C., 2021. Jurassic fast polar shift rejected by a new high-quality paleomagnetic pole from southwest Greenland. Gondwana Res. 97, 240–262. https://doi.org/10.1016/j.gr.2021.05.021.
Laguë, M.M., Pietschnig, M., Ragen, S., Smith, T.A., Battisti, D.S., 2021. Terrestrial evaporation and global climate: lessons from Northland, a planet with a hemispheric continent. J. Clim. 34, 2253–2278. https://doi.org/10.1175/JCLI-D-20-0452.1.
Le Hir, G., Donnadieu, Y., Goddéris, Y., Meyer-Berthaud, B., Ramstein, G., 2011. The climate change caused by the land plant invasion in the Devonian. Earth Planet. Sci. Lett. 310, 203–212. https://doi.org/10.1016/j.epsl.2011.08.042.
Lenton, T.M., Daines, S.J., Mills, B.J.W., 2018. COPSE reloaded: an improved model of biogeochemical cycling over Phanerozoic time. Earth Sci. Rev. 178, 1–28.
Lowenstein, T.K., Kendall, B., Anbar, A.D., 2014. The geologic history of seawater. In: Holland, H.D., Turekian, K.K. (Eds.), Treatise on Geochemistry, Second ed. Elsevier, Oxford, pp. 569–622.
Luthi, D., Le Floch, M., Bereiter, B., Blunier, T., Barnola, J.-M., Siegenthaler, U., Raynaud, D., Jouzel, J., Fischer, H., Kawamura, K., Stocker, T.F., 2008. High-resolution carbon dioxide concentration record 650,000-800,000 years before present. Nature 453, 379–382.
Macdonald, F.A., Swanson-Hysell, N.L., Park, Y., Lisiecki, L., Jagoutz, O., 2019. Arc-continent collisions in the tropics set Earth's climate state. Science 364 (6436), 181.
Manabe, S., Broccoli, A.J., 2020. Beyond Global Warming: How Numerical Models Revealed the Secrets of Climate Change. Princeton University Press.
Manabe, S., Bryan, K., 1985. CO2-induced change in a coupled ocean-atmosphere model and its paleoclimatic implications. J. Geophys. Res. 90 (C6), 11689–11707.
Marks-Peterson, J., Shackleton, S., Higgins, J., Severinghaus, J., Yan, Y., Buizert, C., Kalk, M., Beaudette, R., Hishamunda, V., Eves, D., Carter, A., Kurbatov, A., Epifanio, J., Morgan, J., Nesbitt, I., Bender, M., Brook, E., 2026. Broadly stable atmospheric CO2 and CH4 levels over the past 3 million years. Nature 651 (8106), 647–652.
Mills, B.J.W., Donnadieu, Y., Goddéris, Y., 2021. Spatial continuous integration of Phanerozoic global biogeochemistry and climate. Gondwana Res. 100, 73–86.
Montañez, I.P., 2022. Current Synthesis of the Penultimate Icehouse and Its Imprint on the Upper Devonian through Permian Stratigraphic Record. Geological Society of London, pp. 213–245.
Montañez, I.P., Poulsen, C.J., 2013. The Late Paleozoic Ice Age: an evolving paradigm. Annu. Rev. Earth Planet. Sci. 41, 629–656.
Müller, R.D., Zahirovic, S., Williams, S.E., Cannon, J., Seton, M., Bower, D.J., Tetley, M. G., Heine, C., Le Breton, E., Liu, S., Russell, S.H.J., Yang, T., Leonard, J., Gurnis, M., 2019. A global plate model including lithospheric deformation Along major rifts and orogens since the Triassic. Tectonics 38 (6), 1884–1907.
Muttoni, G., Kent, D.V., 2019. Jurassic monster polar shift confirmed by sequential paleopoles from Adria, promontory of Africa. J. Geophys. Res. Solid Earth 124, 3288–3306. https://doi.org/10.1029/2018JB017199.
Muttoni, G., Kent, D.V., Garzanti, E., Brack, P., Abrahamsen, N., Gaetani, M., 2003. Early Permian Pangea 'B' to Late Permian Pangea 'A'. Earth Planet. Sci. Lett. 215, 379–394.
Muttoni, G., Gaetani, M., Kent, D.V., Sciunnach, D., Angiolini, L., Berra, F., Garzanti, E., Mattei, M., Zanchi, A., 2009a. Opening of the Neo-Tethys Ocean and the Pangea B to Pangea A transformation during the Permian. GeoArabia 14, 17–48.
Muttoni, G., Mattei, M., Balini, M., Zanchi, A., Gaetani, M., Berra, F., 2009b. The drift history of Iran from the Ordovician to the Triassic. Geol. Soc. Lond. Spec. Publ. 312, 7–29.
Muttoni, G., Dallanave, E., Della Porta, G., 2025. European arid anomaly explained with southward drift of Eurasia during the late Jurassic polar shift. Geochem. Geophys. Geosyst. 26 (2), e2024GC011730.
Myhre, G., Highwood, E.J., Shine, K.P., Stordal, F., 1998. New estimates of radiative forcing due to well mixed greenhouse gases. Geophys. Res. Lett. 25 (14), 2715–2718.
Najman, Y., Appel, E., Boudagher-Fadel, M., Bown, P., Carter, A., Garzanti, E., Godin, L., Han, J., Liebke, U., Oliver, G., Parrish, R., Vezzoli, G., 2010. Timing of India–Asia collision: geological, biostratigraphic, and palaeomagnetic constraints. J. Geophys. Res. Solid Earth 115, B12416. https://doi.org/10.1029/2010JB007673.
Olsen, P.E., Laskar, J., Kent, D.V., Kinney, S.T., Reynolds, D.J., Sha, J., Whiteside, J.H., 2019. Mapping solar system chaos with the Geological Orrery. Proc. Natl. Acad. Sci. 116 (22), 10664–10673. https://doi.org/10.1073/pnas.1813901116.
Park, Y., Swanson-Hysell, N.L., Lisiecki, L.E., Macdonald, F.A., 2021. Evaluating the relationship between the area and latitude of Large Igneous Provinces and Earth's long-term climate state. In: Ernst, R.E., Dickson, A.J., Bekker, A. (Eds.), Large Igneous Provinces, Geophysical Monograph Series. American Geophysical Union, Washington DC, pp. 153–168.
Parrish, J.T., 1993. Climate of the supercontinent Pangea. J. Geol. 101, 215–233.
Rampino, M.R., Caldeira, K., Rodriguez, S., 2024. Sixteen mass extinctions of the past 541 My correlated with 15 pulses of Large Igneous Province (LIP) volcanism and the 4 largest extraterrestrial impacts. Glob. Planet. Chang. 234, 104369.
Raup, D.M., 1986. Biological extinction in Earth history. Science 231, 1528–1533.
Rowley, D.B., 2002. Rate of plate creation and destruction: 180 Ma to present. Geol. Soc. Am. Bull. 114, 927–933.
Royer, D.L., Berner, R.A., Montanez, I.P., Tabor, N.J., Beerling, D.J., 2004. CO2 as a primary driver of Phanerozoic climate. GSA Today 14, 4–10.
Schoene, B., Eddy, M.P., Samperton, K.M., Keller, C.B., Keller, G., Adatte, T., Khadri, S.F. R., 2019. U-Pb constraints on pulsed eruption of the Deccan Traps across the end-Cretaceous mass extinction. Science 363 (6429), 862.
Schulte, P., Alegret, L., Arenillas, I., Arz, J.A., Barton, P.J., Bown, P.R., Bralower, T.J., Christeson, G.L., Claeys, P., Cockell, C.S., Collins, G.S., Deutsch, A., Goldin, T.J., Goto, K., Grajales-Nishimura, J.M., Grieve, R.A.F., Gulick, S.P.S., Johnson, K.R., Kiessling, W., Koeberl, C., Kring, D.A., MacLeod, K.G., Matsui, T., Melosh, J., Montanari, A., Morgan, J.V., Neal, C.R., Nichols, D.J., Norris, R.D., Pierazzo, E., Ravizza, G., Rebolledo-Vieyra, M., Reimold, W.U., Robin, E., Salge, T., Speijer, R.P., Sweet, A.R., Urrutia-Fucugauchi, J., Vajda, V., Whalen, M.T., Willumsen, P.S., 2010. The chicxulub asteroid impact and mass extinction at the Cretaceous-Paleogene boundary. Science 327, 1214–1218.
Sepkoski, J.J., 1996. Patterns of phanerozoic extinction: a perspective from global data bases. In: Walliser, O.H. (Ed.), Global Events and Event Stratigraphy in the Phanerozoic. Springer, Berlin Heidelberg, pp. 35–51.
Siler, N., Roe, G.H., Armour, K.C., 2018. Insights into the zonal-mean response of the hydrologic cycle to global warming from a diffusive energy balance model. J. Clim. 31, 7481–7500. https://doi.org/10.1175/JCLI-D-18-0081.

Sprain, C.J., Renne, P.R., Vanderkluysen, L., Pande, K., Self, S., Mittal, T., 2019. The eruptive tempo of Deccan volcanism in relation to the Cretaceous-Paleogene boundary. Science 363 (6429), 866.

Stephens, G.L., O'Brien, D., Webster, P.J., Pilewski, P., Kato, S., Li, J.-L., 2015. The Albedo of Earth. Rev. Geophys. 53, 141–163. https://doi.org/10.1002/2014RG000449.

Strother, P.K., Traverse, A., Vecoli, M., 2015. Cryptospores from the Hanadir Shale Member of the Qasim Formation, Ordovician (Darriwilian) of Saudi Arabia: taxonomy and systematics. Rev. Palaeobot. Palynol. 212, 97–110. https://doi.org/10.1016/j.revpalbo.2014.08.018.

Torsvik, T.H., Van der Voo, R., Preeden, U., Mac Niocaill, C., Steinberger, B., Doubrovine, P.V., van Hinsbergen, D.J.J., Domeier, M., Gaina, C., Tohver, E., Meert, J.G., McCausland, P.J.A., Cocks, L.R.M., 2012. Phanerozoic polar wander, palaeogeography and dynamics. Earth Sci. Rev. 114, 325–368.

Torsvik, T.H., Royer, D.L., Marcilly, C.M., Werner, S.C., 2024. User-friendly carbon-cycle modelling and aspects of Phanerozoic climate change. Appl. Comput. Geosci. 23, 100180.

Veizer, J., Godderis, Y., Francois, L.M., 2000. Evidence for decoupling of atmospheric CO2 and global climate during the Phanerozoic eon. Nature 408, 698–701.

Walker, J.C.G., Hays, P.B., Kasting, J.F., 1981. A negative feedback mechanism for the long-term stabilization of Earth's surface-temperature. J. Geophys. Res.-Atmos. 86, 9776–9782.

Yi, Z., Liu, Y., Meert, J.G., 2019. A true polar wander trigger for the Great Jurassic East Asian Aridification. Geology 47 (12), 1112–1116.

Zhang, Y., Yuan, S., Mills, B.J.W., Merdith, A.S., Hu, Y., Zhu, M., 2025. Increased continental exposure as a Driver of carbon drawdown and initiation of the Late Paleozoic ice age. Geophys. Res. Lett. 52 (24), e2025GL119356.